RESEARCH ARTICLE
SPACE PHYSICS: IONOSPHERIC PHYSICS

Earth and Planetary Physics
9: 731–739, 2025
doi: 10.26464/epp2025052

Ionospheric F-region currents estimated from Macau Science Satellite-1 and Swarm satellite magnetic data

JuYuan Xu*, HongBo Yao, and Keke Zhang

Macau Institute of Space Technology and Application, Macau University of Science and Technology, Taipa, Macao 999078, China

Key Points:

- New models of ionospheric F-region currents and associated magnetic field are estimated from MSS-1 (Macau Science Satellite-1) and Swarm magnetic data.
- These models successfully capture the primary spatial structures and seasonal variations of ionospheric F-region currents.
- The method and models presented here are essential for comprehensive geomagnetic field modeling.

Citation: Xu, J. Y., Yao, H. B., and Zhang, K. (2025). Ionospheric F-region currents estimated from Macau Science Satellite-1 and Swarm satellite magnetic data. *Earth Planet. Phys.*, *9*(3), 731–739. http://doi.org/10.26464/epp2025052

Abstract: Accurate modeling of Earth's ionospheric F-region currents is essential for refining geomagnetic field models and understanding magnetosphere-ionosphere coupling. In this study, we develop averaged models to characterize F-region currents using magnetic data from the MSS-1 (Macau Science Satellite-1) and Swarm satellite missions. Our approach employs a toroidal field representation, utilizing spherical harmonics to capture spatial variations and Fourier series to represent temporal dynamics. Two models, *Model-A* and *Model-B*, derived from distinct datasets, are constructed to represent current patterns at altitudes of 450 km and 512 km, respectively. Our models successfully capture the primary spatial structures and seasonal variations of polar field-aligned currents. Additionally, they accurately reproduce the localized inter-hemispheric field-aligned currents observed in mid and low latitudes during solstices, particularly between 14:00 and 16:00 magnetic local times. These findings enhance our understanding of ionospheric F-region currents and contribute to more precise geomagnetic field modeling.

Keywords: Macau Science Satellite-1; Swarm; field-aligned currents; geomagnetism; ionosphere

1. Introduction

Near-Earth magnetic field, resulting from contributions from various sources (Hulot et al., 2015), is highly complex. Geomagnetic field modeling enables the separation of these different magnetic signals from observational data, allowing for individual study of each source (Olsen and Stolle, 2012). A significant challenge in achieving high-precision geomagnetic models is accounting for the magnetic fields generated by ionospheric currents (Finlay et al., 2017).

Ionospheric currents are stratified by altitude into two principal layers. In the E-region (90–150 km), dominant systems include the solar-quiet (*Sq*) currents — dual hemispheric vortices driven by solar heating — and the equatorial electrojet (EEJ). The F-region (150–1000 km), in contrast, hosts field-aligned currents (FACs) that flow along geomagnetic field lines. Polar FACs, first characterized by Iijima and Potemra(1976a, b), connect the magnetosphere to the ionosphere and are driven by solar wind interactions. In the mid- and low-latitude region, interhemispheric FACs, first theorized by Van Sabben (1966, 1970), arise from hemispheric asymmetries in *Sq* currents and were later confirmed via satellite observations (Olsen, 1997).

Several dedicated models have advanced our understanding of polar FACs. Notable examples include MFACE (He MS et al., 2012), AMPS (Average Magnetic field and Polar current System) (Laundal et al., 2018), and the EW-FAC model (Edwards et al., 2020). Research on polar FACs consistently shows that both the distribution and intensity of these current systems are highly influenced by interplanetary magnetic field (IMF) conditions and solar wind plasma (Ganushkina et al., 2015; Carter et al., 2016). Additionally, inter-hemispheric FACs have been extensively studied (Lühr et al., 2019; Park et al., 2020; Wang FJ et al., 2022; Fillion et al., 2023). Co-estimating all magnetic sources in a single step is ideal yet complex, as demonstrated by the Comprehensive Model (CM) series (Sabaka et al., 2002, 2020). In CM5 (Sabaka et al., 2015), a toroidal field is used to describe the magnetic field generated by F-region currents, successfully capturing their slowly varying components.

A critical challenge in characterizing F-region currents arises from the limited local time sampling of polar-orbiting satellites. For example, Swarm-A requires approximately 133 days to achieve full 24-hour local time coverage — a significant limitation given the strong diurnal variability of these currents. The Macau Science

Correspondence to: J. Y. Xu, juyuanxu@must.edu.mo
Received 15 JAN 2025; Accepted 20 MAR 2025.
First Published online 16 APR 2025.

Satellite-1 (MSS-1), operating in a low-inclination orbit, can provide denser local time sampling over shorter timescales (Zhang K, 2023). This enhanced temporal resolution, particularly in low- and mid-latitude regions, enables improved characterization of current systems that vary substantially with local solar time.

In this study, we develop preliminary models of ionospheric F-region currents using magnetic data from MSS-1 and Swarm satellites. Given that MSS-1 has been operational for only a year and a half, our research aims to determine whether key characteristics of F-region currents can be recovered from MSS-1 and Swarm data, thereby improving our understanding of these critical current systems.

2. Data

2.1 Satellite Magnetic Data

We use vector magnetic field observations from both the Swarm and MSS-1 missions. For the Swarm mission, we utilize vector data from Swarm-A (Alpha) and Swarm-B (Bravo), versions 0602/0605/0606, spanning November 26, 2013 through June 30, 2024. For MSS-1, we use vector data from the MSS-1A satellite, versions V04**, from November 2, 2023 through June 30, 2024. All vector data are downsampled to one-minute intervals and used in the North–East–Center (NEC) coordinate frame, as provided in the data products.

2.2 Data Selection

We select data reflecting geomagnetic quiet periods based on the following criteria:

- *Kp* index: $Kp < 2^{\circ}$ (Matzka et al., 2021).
- Ring current index (*RC*): The change in *RC* is no more than 2 nT/h, i.e., $|\mathrm{d}RC/\mathrm{d}t| \le 2$ nT/h (Olsen et al., 2014).
- Merging electric field (E_m): E_m averaged over the previous 2 h is less than 0.8 mV/m. i.e., $E_m \le 0.8$ mV/m (Newell et al., 2007).
- Interplanetary magnetic field (B_z): B_z averaged over the previous 2 h is positive.

We do not limit our dataset to nighttime conditions; instead, we include observations from all local times to achieve uniform sampling of F-region currents. After applying these criteria, we obtain 1,271,670 vector observations from Swarm-A, 1,274,226 from Swarm-B, and 60,453 from MSS-1.

2.3 Data Processing

To isolate the magnetic signature of ionospheric F-region currents, we subtract predictions of other magnetic contributions from the raw observations ($\boldsymbol{B}_{\mathrm{obs}}$). Specifically, we remove the core ($\boldsymbol{B}_{\mathrm{core}}$), lithospheric ($\boldsymbol{B}_{\mathrm{lith}}$), and large-scale magnetospheric ($\boldsymbol{B}_{\mathrm{mag}}$) field contributions based on the CHAOS-7.18 model (Finlay et al., 2020). We also remove the ionospheric solar-quiet (*Sq*) and equatorial electrojet (EEJ) field ($\boldsymbol{B}_{\mathrm{iono}}$) estimated by the DIFI-7 model (Chulliat et al., 2016). The residuals — observed data minus these model predictions — are used as the input data for modeling F-region currents, which can be expressed as:

$$\delta\boldsymbol{B} = \boldsymbol{B}_{\mathrm{obs}} - \boldsymbol{B}_{\mathrm{core}} - \boldsymbol{B}_{\mathrm{lith}} - \boldsymbol{B}_{\mathrm{mag}} - \boldsymbol{B}_{\mathrm{iono}}. \quad (1)$$

The reliability of these residuals depends critically on the accuracy of the *Sq* and EEJ predictions from the DIFI model. Residual signals in non-polar regions require particular attention, as their weaker amplitude makes them more susceptible to errors in these background field removals compared to stronger polar signals.

We divide these data into two datasets. The data from Swarm-A and MSS-1 are referred to as dataset A, while the data from Swarm-B is referred to as dataset B. These two datasets can be regarded as measurements from two distinct orbital shells. Figure 1 shows mean altitude (curve) and altitude range (shaded region) of the satellites with respect to time. We model these two datasets separately, which will be further introduced in Section 3.4.

3. Model Parametrization and Estimation

3.1 Toroidal–Poloidal Decomposition of the Magnetic Field Perturbation

Building upon the methodology of Olsen (1997) and partially based on Backus (1986), we consider the theorem that any solenoidal (divergence-free) vector field can be uniquely decomposed into toroidal and poloidal components on a sphere.

Given that the magnetic field is divergence-free, i.e., $\nabla \cdot \delta\boldsymbol{B} = 0$, the perturbation of the magnetic field $\delta\boldsymbol{B}$ can be expressed as the sum of toroidal and poloidal components:

$$\delta\boldsymbol{B} = \delta\boldsymbol{B}_{\mathrm{tor}} + \delta\boldsymbol{B}_{\mathrm{pol}} = \nabla \times (T\boldsymbol{r}) + \nabla \times \nabla \times (P\boldsymbol{r}), \quad (2)$$

where T and P are scalar functions representing the toroidal and poloidal potentials, respectively, and $\boldsymbol{r}$ is the position vector.

Backus (1986) demonstrated that for a thin shell whose thickness is small compared to its mean radius, the poloidal component of the magnetic field perturbation $\delta\boldsymbol{B}_{\mathrm{pol}}$ tends to zero. This approximation is valid for geomagnetic satellites sampling the Earth's magnetic field at satellite altitudes and is adopted here. Consequently, the magnetic field perturbation simplifies to:

$$\delta\boldsymbol{B} = \nabla \times (T\boldsymbol{r}), \quad (3)$$

with the associated current density:

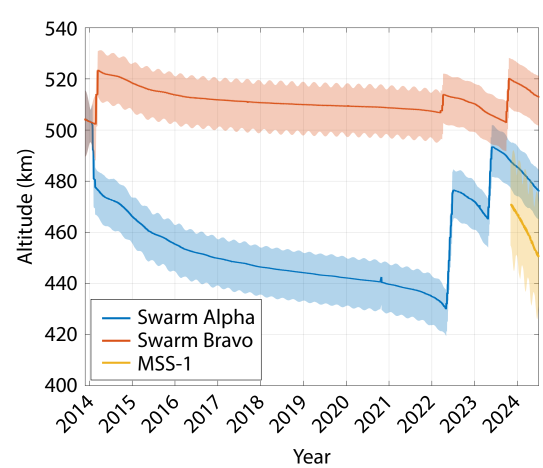

Figure 1. Altitude (with respect to a mean geocentric radius of a = 6371.2 km) of the Swarm and MSS-1 satellites as a function of time. The shaded regions indicate the altitude range.

$$\mu_0 \boldsymbol{J} = \nabla \times \nabla \times (T\boldsymbol{r}). \tag{4}$$

3.2 Basis Function Selection

We base the parametrization of the toroidal scalar potential T on the CM3 model (Sabaka et al., 2000, 2002), introducing some modifications to suit our study. Specifically, we employ spherical harmonics to describe the spatial variation and Fourier series to represent the temporal variation. In the dipole coordinate system, the toroidal scalar T can be expanded as:

$$\begin{aligned} T(t, t_{\mathrm{mut}}, r, \theta_d, \phi_d) = \sum_{s=0}^{2}\sum_{p=0}^{4}\sum_{n=1}^{60}\sum_{m=0}^{12}\left(\frac{a}{r}\right)P_n^m(\cos\theta_d) \\ \left\{\left[\varphi_{n,s,p}^{m,(c)}\cos(m\phi_d) + \psi_{n,s,p}^{m,(c)}\sin(m\phi_d)\right]\cos(\omega_s st + \omega_p pt_{\mathrm{mut}}) \right. \\ \left. + \left[\varphi_{n,s,p}^{m,(s)}\cos(m\phi_d) + \psi_{n,s,p}^{m,(s)}\sin(m\phi_d)\right]\sin(\omega_s st + \omega_p pt_{\mathrm{mut}})\right\}, \end{aligned} \tag{5}$$

where t (expressed in yrs) is the decimal years counted from January 1st, at 00:00 universal time, t_{mut} (expressed in hrs) is the magnetic universal time (MUT), $a = 6371.2$ km is the mean surface radius of the Earth, r is the radius, θ_d and ϕ_d are, respectively, dipole colatitude and longitude, P_n^m are the associated Legendre functions using the Schmidt semi-normalization (Winch et al., 2005), $\omega_s = 2\pi$ rads/yr is the fundamental angular frequency for seasonal variation, $\omega_p = 2\pi/24$ rads/hr is the fundamental angular frequency for diurnal variation, s and p are the associated wavenumbers and $\varphi_{n,s,p}^{m,(c)}$, $\psi_{n,s,p}^{m,(c)}$, $\varphi_{n,s,p}^{m,(s)}$ and $\psi_{n,s,p}^{m,(s)}$ are the expansion coefficients.

The dipole coordinate system is defined based on the Earth's magnetic dipole axis (Laundal and Richmond, 2017). In this study, we use the 12th generation of the International Geomagnetic Reference Field (IGRF) (Thébault et al., 2015) at epoch 2015.0 as the reference model to calculate the dipole axis.

Following Sabaka et al. (2015), to capture small-scale features of F-region currents, we set the maximum degree (n) and order (m) of the spherical harmonics to 60 and 12, respectively. To represent the dominant periods in the diurnal and seasonal spectra, we set the diurnal wavenumbers to $p = 0, 1, 2, 3, 4$ and the seasonal wavenumbers to $s = 0, 1, 2$.

For clarity, we briefly discuss the concepts of magnetic local time (MLT) and magnetic universal time. The magnetic local time t_{mlt} is defined as:

$$t_{\mathrm{mlt}} = (\phi_d - \phi_{d,\hat{s}})/15 + 12, \tag{6}$$

where ϕ_d is the dipole longitude, in degrees, of the point in question, $\phi_{d,\hat{s}}$ is the dipole longitude, in degrees, of the subsolar point, and $t_{\mathrm{mlt}} \in [0, 24)$ is in hours. The subsolar point depends only on the time and date. MLT is useful for describing external fields whose current systems exhibit diurnal cycles and are also influenced by Earth-fixed internal fields. The MUT is defined as the MLT at the dipole prime meridian, given by:

$$t_{\mathrm{mut}} = -\phi_{d,\hat{s}}/15 + 12, \tag{7}$$

which is equivalent to setting $\phi_d = 0$ in Equation (6).

It is important to emphasize the radial dependence in Equation (5). The radial dependence given by a/r makes vanishing horizontal components of currents ($J_\theta = J_\phi = 0$), resulting in purely radial currents. For satellite data measured in the F-region ionosphere, the assumption of radial currents is suitable for describing polar field-aligned currents (Olsen, 1997).

With the expression of toroidal scalar T, the model prediction of the toroidal field in geocentric spherical coordinates is given by:

$$\delta \boldsymbol{B}_{\mathrm{GEO}} = \boldsymbol{R}_{\mathrm{GEO}\leftarrow\mathrm{MAG}}[\nabla_{\mathrm{MAG}} \times (T\boldsymbol{r})], \tag{8}$$

where $\boldsymbol{R}_{\mathrm{GEO}\leftarrow\mathrm{MAG}}$ is a rotation matrix from dipole spherical to geocentric spherical coordinates, ∇_{MAG} is the gradient operator in dipole spherical coordinates.

3.3 Model Estimation

The model parameters are represented as a column vector, denoted by $\boldsymbol{m}$. These parameters are estimated by minimizing a quadratic cost function defined as:

$$\Phi(\boldsymbol{m}) = [\boldsymbol{d} - \boldsymbol{g}(\boldsymbol{m})]^{\mathrm{T}} \boldsymbol{W} [\boldsymbol{d} - \boldsymbol{g}(\boldsymbol{m})] + \lambda \boldsymbol{m}^{\mathrm{T}} \boldsymbol{\Lambda} \boldsymbol{m}, \tag{9}$$

where $\boldsymbol{g}(\boldsymbol{m}_k) = \boldsymbol{G}\boldsymbol{m}_k$ predicts the model outcomes (Equation (8)), $\boldsymbol{d}$ is the vector of observed data in geocentric spherical coordinates, $\boldsymbol{W}$ is the data weighting matrix, λ regulates the strength of regularization, and $\boldsymbol{\Lambda}$ is the regularization matrix.

Due to the complexities introduced by updating the data weighting matrix and incorporating regularization, minimizing the cost function is a non-linear problem. To address this, we employ a Newton-type algorithm that iteratively updates the model parameter vector. At each kth iteration, the parameter vector updates as follows:

$$\boldsymbol{m}_{k+1} = \boldsymbol{m}_k + (\boldsymbol{G}^{\mathrm{T}}\boldsymbol{W}_k\boldsymbol{G} + \lambda\boldsymbol{\Lambda})^{-1}\left\{\boldsymbol{G}^{\mathrm{T}}\boldsymbol{W}_k[\boldsymbol{d} - \boldsymbol{g}(\boldsymbol{m}_k)] - \lambda\boldsymbol{\Lambda}\boldsymbol{m}_k\right\}, \tag{10}$$

with $\boldsymbol{G}$ representing the matrix of partial derivatives of the residuals with respect to the model parameters. For the initial solution $\boldsymbol{m}_0$, all the parameters are set to zero. The model is considered to have converged when the parameters change only slightly between successive iterations, defined by the criterion:

$$\frac{||\boldsymbol{m}_{k+1} - \boldsymbol{m}_k||}{||\boldsymbol{m}_k||} < 0.01. \tag{11}$$

3.3.1 Data weighting

The data weighting matrix $\boldsymbol{W}_k$ is composed of three components: the data error covariance weight, the robust Huber weight, and a weight to adjust for the high data density in polar regions. The weight for each data point d_i is calculated as:

$$w_i = \frac{\min(c/\varepsilon_{i,k}, 1)\cdot\sin\theta}{\sigma_i^2}, \tag{12}$$

where $c = 1.5$, $\varepsilon_{i,k} = (d_i - g_i(\boldsymbol{m}_k))/\sigma_i$ is the normalized residual of the ith data in the kth iteration and σ_i represents the data error. We assess both observation error and errors caused by unmodeled sources, and set all the data errors to 5 nT. The Huber weight, $\min(c/\varepsilon_{i,k}, 1)$, aids in achieving a robust solution while data exhibits long-tailed error distributions. The term $\sin\theta$ (where θ is the geocentric colatitude) helps in balancing the over-representation of data from polar regions. These various weights are assembled into the diagonal matrix $\boldsymbol{W}_k$.

3.3.2 Model regularization

The regularization matrix $\boldsymbol{\Lambda}$ encourages smoother solutions by penalizing sharp gradients in the model parameters. This diagonal matrix applies a quadratic penalty scaled by the regularization parameter. Specifically, we use the mean-square magnitude of the surface Laplacian of J_r at a reference altitude h_R averaged over time T and the full spherical domain:

$$\boldsymbol{m}^\mathrm{T}\boldsymbol{\Lambda}\boldsymbol{m} = \frac{\int_0^T \int_\Omega [\nabla_s^2 J_r(t, t_\mathrm{mut}, h_\mathrm{R}, \theta_d, \phi_d)]^2 \mathrm{d}\Omega \mathrm{d}t}{\int_0^T \int_\Omega \mathrm{d}\Omega \mathrm{d}t}, \tag{13}$$

where ∇_s^2 is the horizontal part of the Laplacian operator, which is defined as:

$$\nabla_s^2 = \frac{1}{r^2 \sin\theta_d} \frac{\partial}{\partial\theta_d}\left(\sin\theta_d \frac{\partial}{\partial\theta_d}\right) + \frac{1}{r^2 \sin^2\theta_d} \frac{\partial^2}{\partial\phi_d^2}, \tag{14}$$

and J_r is given by:

$$\begin{aligned} &J_r(t, t_\mathrm{mut}, h_\mathrm{R}, \theta_d, \phi_d) \\ &= \frac{1}{\mu_0(a+h_\mathrm{R})} \sum_{s=0}^{2} \sum_{p=0}^{4} \sum_{n=1}^{60} \sum_{m=0}^{12} n(n+1) \left(\frac{a}{a+h_\mathrm{R}}\right) P_n^m(\cos\theta_d) \\ &\left\{ \left[\varphi_{n,s,p}^{m,(c)} \cos(m\phi_d) + \psi_{n,s,p}^{m,(c)} \sin(m\phi_d)\right] \cos(\omega_s st + \omega_p pt_\mathrm{mut}) \right. \\ &\left. + \left[\varphi_{n,s,p}^{m,(s)} \cos(m\phi_d) + \psi_{n,s,p}^{m,(s)} \sin(m\phi_d)\right] \sin(\omega_s st + \omega_p pt_\mathrm{mut}) \right\}. \end{aligned} \tag{15}$$

We take $T = 1$ yr to access J_r in a maximum period. After testing various values, we set $\lambda = 1.0 \times 10^{-4} (\mathrm{nA} \cdot \mathrm{m}^{-4})^{-2}$, striking a balance between fitting the data closely and maintaining a smooth solution. By enforcing smoothness, this regularization reduces unrealistic spatial fluctuations in J_r.

3.4 Model Settings

We develop two models to capture ionospheric F-region currents at different altitudes. The first model, *Model-A*, is derived from dataset A (Swarm-A and MSS-1 data) at $h_\mathrm{R} = 450$ km. The second, *Model-B*, is derived from dataset B (Swarm-B data) at $h_\mathrm{R} = 512$ km. Except for their datasets used for modeling and the altitude-dependent regularization, the models are essentially identical. The differences in their configurations reflect the distinct current patterns observed at different orbital heights. Note that our models are still radially dependent, however, their individual configurations influence their sensitivity to ionospheric currents at different altitudes.

It is important to note that we assume a purely toroidal magnetic field for a thin sampled shell, which corresponds to a purely poloidal current. Therefore, only the B_θ and B_ϕ components are used for modeling. Figure 2 presents histograms of the field components from datasets A and B. The data reveals that the root mean square (RMS) values of B_θ and B_ϕ are significantly higher than that of B_r in both datasets, indicating that magnetic field perturbations at these altitudes are predominantly concentrated in the horizontal components.

4. Results

4.1 Residual Statistics

Tables 1 and 2 summarize the residual statistics for *Model-A* and *Model-B*, respectively. We use quasi-dipole (QD) latitude λ_QD to distinguish different regions (Richmond, 1995). The data are categorized into low latitudes ($|\lambda_\mathrm{QD}| \le 30°$), middle latitudes ($30° < |\lambda_\mathrm{QD}| \le 55°$), and high latitudes ($|\lambda_\mathrm{QD}| > 55°$). Both models exhibit similar residual statistics, with the highest RMS values occurring at high latitudes. This trend reflects the complex current systems present in polar regions.

The elevated RMS values at high latitudes are primarily due to the polar electrojets and some high-frequency currents, which are not accounted for in our models. These currents can induce magnetic perturbations ranging from several hundred to thousands of nT, complicating the accurate fitting of magnetic data in polar areas compared to non-polar regions. Despite these challenges, our models successfully capture the average temporal and spatial characteristics of F-region currents.

Our models have a maximum period of one year but are derived from 11 years of data, so the quality of the fit may vary across individual years. Using *Model-A* and Swarm-A data as an example, Figure 3 shows the annual average of the weighted RMS and the solar radiation index $F_{10.7}$ from 2014 to 2024. The $F_{10.7}$ index (in

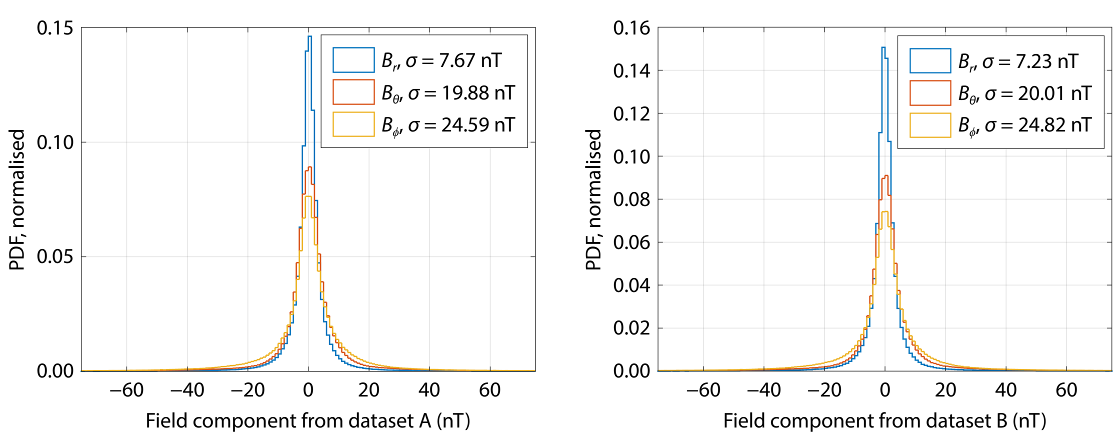

Figure 2. Histograms of field components from dataset A (left) and dataset B (right). The bin width is 1 nT, and the histograms are normalized to integrate to a unit area. Values outside the range of ±75 nT are not displayed but are included in the normalization. RMS values are indicated in the legend.

Table 1. Residual statistics for *Model-A* using data from Swarm-A and MSS-1. The mean and RMS values represent the Huber-weighted mean and Huber-weighted root mean square of the deviations from the mean, respectively.

Satellite	QD latitude	Component	Number	Mean (nT)	RMS (nT)
Swarm-A	Low	B_θ	415518	0.17	3.94
		B_ϕ	415518	−0.05	6.19
	Middle	B_θ	368226	0.78	4.09
		B_ϕ	368226	0.01	4.45
	High	B_θ	487926	0.81	11.93
		B_ϕ	487926	0.02	13.24
MSS-1	Low	B_θ	34100	0.71	5.19
		B_ϕ	34100	0.14	6.74
	Middle	B_θ	26353	0.56	4.87
		B_ϕ	26353	0.13	5.03

Table 2. Residual statistics for *Model-B* using data from Swarm-B. The mean and RMS values represent the Huber-weighted mean and Huber-weighted root mean square of the deviations from the mean, respectively.

Satellite	QD latitude	Component	Number	Mean (nT)	RMS (nT)
Swarm-B	Low	B_θ	417095	0.14	3.83
		B_ϕ	417095	−0.03	6.01
	Middle	B_θ	368126	0.68	4.01
		B_ϕ	368126	0.02	4.43
	High	B_θ	489005	0.70	11.79
		B_ϕ	489005	0.01	13.19

solar flux units, sfu ≡ 10^{-22} W m^{-2} Hz^{-2}) serves as an indicator of solar cycle intensity. As shown in Figure 3, the consistency between the weighted RMS and $F_{10.7}$ index over time reflects well the influence of solar activity on our model fitting. As the figure illustrates, the RMS closely tracks solar activity: the lowest RMS occurs between 2018 and 2020 (solar minimum). This result can be explained by the dependence of ionospheric current intensity on solar flux.

4.2 Magnetic Field Generated by F-region Currents

Figure 4 displays the magnetic field maps produced by F-region currents as derived from our models. Both *Model-A* and *Model-B* yield similar results. For the south and east components, magnetic field amplitudes in high latitude regions exceed 30 nT, significantly higher than the approximately 5 to 10 nT observed in mid and low latitude regions. In these lower latitudes, the magnetic field intensity is markedly greater on the dayside compared to the nightside. On the dayside, the magnetic field patterns are primarily aligned along the magnetic equator. Notably, in the east component, a negative patch is observed over central Africa during local midday.

These findings illustrate the typical characteristics of magnetic fields generated by F-region currents, demonstrating that our models capture these essential features.

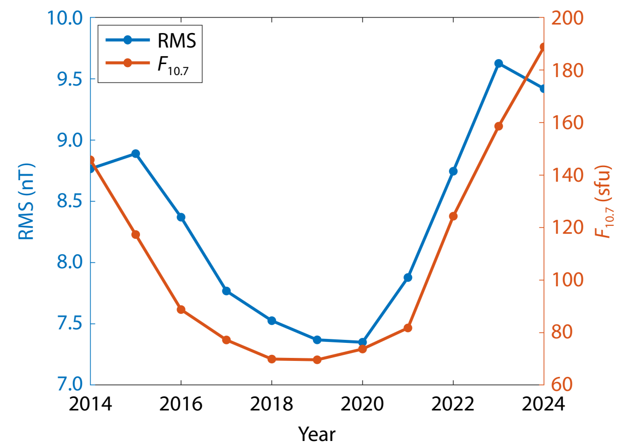

Figure 3. Annual average of RMS (from the Swarm-A residuals of Model A) and $F_{10.7}$ index from 2014 to 2024.

4.3 Local Time Variations of F-region Currents

In this section, we present the local time variations of the radial component J_r of the ionospheric F-region currents as derived from our models. Utilizing a specialized colorbar to differentiate current intensities across various latitudes (Sabaka et al., 2015), Figure 5 displays the estimates of J_r for *Model-A* (at an altitude of 450 km) and *Model-B* (at 512 km) across different MLTs.

Both models indicate that current intensity is markedly higher in polar regions compared to mid and low latitudes, with peak values exceeding 100 nA/m^2. These high-intensity currents are primarily associated with region-1 (R1) and region-2 (R2) field-aligned currents, which will be discussed in the next section. In contrast, at low and middle latitudes, J_r is generally negligible during local midnight (00 MLT) and dawn (06 MLT). The current strength increases toward noon (12 MLT) to approximately 10 nA/m^2 and then gradually diminishes by dusk (18 MLT). Notably, around noon (12 MLT), there are numerous symmetric patches along the magnetic equator with opposite current directions, which likely correspond to inter-hemispheric field-aligned currents.

We anticipate that *Model-A* and *Model-B* would exhibit differences in current patterns due to their distinct sampling altitudes. However, as shown in Figure 5, the differences are minimal. The large-scale current patterns in both models are remarkably similar, likely because the sampling altitudes of the two models are very close. Additionally, these current patterns closely resemble those observed in the CHAMP sampling shell in the CM5 model, which also operates around an altitude of 450 km. Despite using different datasets, the local time variations of the modeled currents are comparable to those in CM5, possibly due to similar parameterization approaches (Sabaka et al., 2015).

4.4 Polar Field-aligned Currents

In this section, we present the spatial distribution and seasonal variations of the estimated field-aligned currents in the polar regions derived from *Model-A*. Figure 6 illustrates the polar distri-

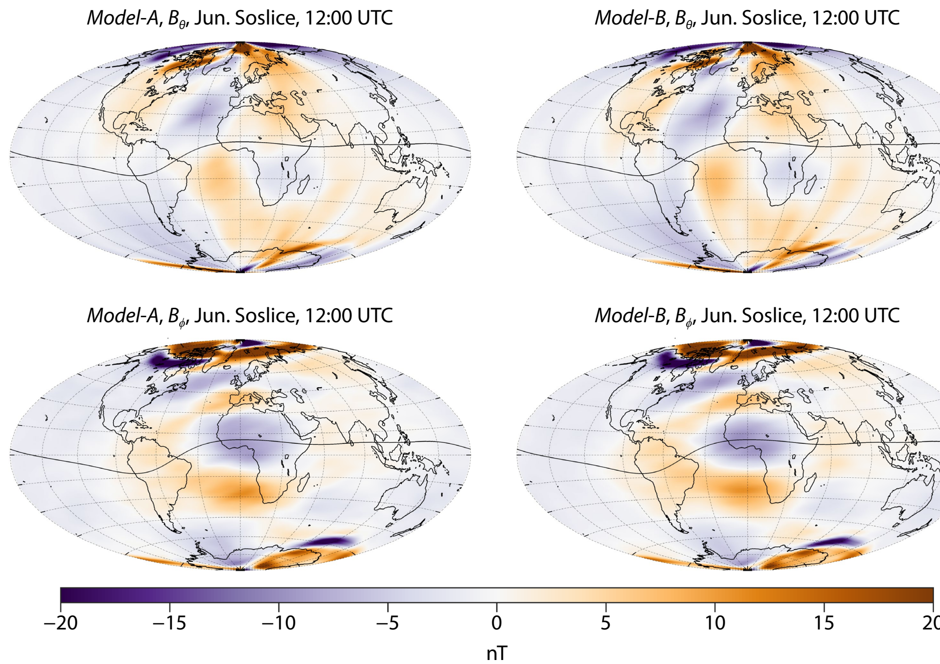

Figure 4. South component (top) and east component (bottom) of the magnetic field generated by F-region currents, derived from *Model-A* (left) and *Model-B* (right) at 12:00 UTC during the June solstice. The altitudes of the maps are 450 km for *Model-A* and 512 km for *Model-B*. The dipole equator is outlined with a black contour.

bution of field-aligned currents densities in both the Northern and Southern hemispheres across different seasons, as calculated by *Model-A*.

It is important to note that these results specifically represent FACs under geomagnetically quiet conditions and with northward interplanetary magnetic field (IMF), differing from cases without data selection (e.g., Xiong C et al., 2023). The polar field-aligned currents exhibit distinct concentric patterns, identified as R1 and R2 currents (Iijima and Potemra, 1976a). The spatial structure of these currents remains relatively consistent within each hemisphere. Seasonally, current densities are lower during local winter compared to summer and equinox periods, aligning with observations from DMSP satellites (Ohtani et al., 2005). This seasonal variation can be attributed to changes in ionospheric conductivity. The locations of maximum current typically occur on the dayside, near noon.

Our model also identifies an additional current system. During the summer solstices in both hemispheres, a pair of currents with opposite directions is observed in the dayside of the polar region between 6 and 18 MLT. These currents, referred to as NBZ currents (or region-0 currents), are prominent in summer and are associated with strong northward interplanetary magnetic fields (Stauning, 2002; He MS et al., 2012).

The averaging effect of our model and the focus on geomagnetic quiet periods result in relatively low current densities and broader current patterns compared to dedicated models for field-aligned currents, such as EW-FAC (Edwards et al., 2020) and MFACE (He MS et al., 2012). Overall, our models successfully capture the primary spatial structures and seasonal variations of polar field-aligned currents.

4.5 Inter-hemispheric Field-aligned Currents

In this section, we examine the inter-hemispheric field-aligned currents in mid and low latitude regions derived from *Model-A*. Figure 7 displays the radial component J_r estimates during the June and December solstices for magnetic local times between 14:00 and 16:00.

As shown in Figure 7, during the June solstice, large-scale currents with densities ranging from 2 to 10 nA/m^2 predominantly flow from regions over North America to regions over South America. Conversely, during the December solstice, the currents mainly flow from regions over the northern Pacific to regions over the southern Pacific. These inter-hemispheric field-aligned currents are driven by seasonal variations in wind patterns and ionospheric conductivity (Fukushima, 1994; Olsen, 1997). Our results highlight both the seasonal changes and localized characteristics of these currents.

5. Conclusions

In this study, we developed averaged models to characterize the radial currents in the ionospheric F-region using magnetic data from the MSS-1 and Swarm satellites. Our models utilize a toroidal field representation to capture the magnetic signals induced by F-region currents, employing spherical harmonics for spatial variations and Fourier series for temporal dynamics. *Model-A* and *Model-B*, derived from distinct datasets, provide current patterns at different altitudes.

The analysis of polar currents demonstrates that our models effectively capture the primary spatial structures and seasonal variations of polar field-aligned currents. Additionally, at mid and low latitudes, our models successfully reproduce the localized features of inter-hemispheric field-aligned currents during solstices, particu-

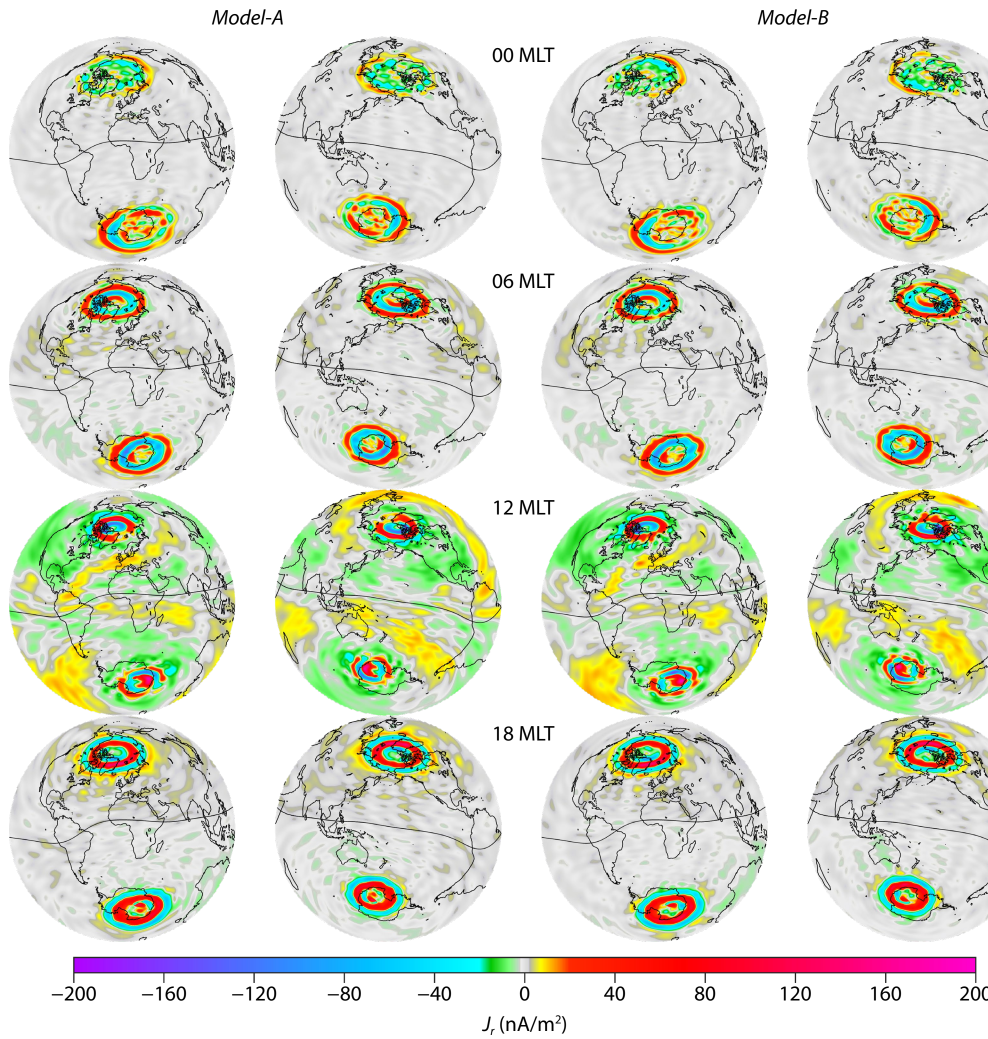

Figure 5. Radial component J_r of the ionospheric F-region currents during the September equinox for different magnetic local times (MLT) derived from *Model A* (left pairs) and *Model B* (right pairs). Each pair consists of two azimuthal equidistant projections centred at 0° (left member) and 180° (right member) longitude. Each map represents J_r at a specific MLT across all spatial locations. The magnetic equator is outlined with a black contour.

larly evident between 14:00 to 16:00 magnetic local times. These results confirm that our models accurately represent key aspects of the ionospheric F-region current systems across various latitudes and temporal conditions.

Data Availability

The data underlying this paper are available in the following repositories:

(1) Swarm data is available through ESA at https://swarm-diss.eo.esa.int/.

(2) The MSS-1 data is available at https://mss.must.edu.mo/data.html.

(3) *RC* index is available at http://www.spacecenter.dk/files/magnetic-models/RC/.

(4) Solar wind speed, interplanetary magnetic field and *Kp* index are available through the GSFC/SPDF OMNIWeb interface at https://omniweb.gsfc.nasa.gov/.

(5) CHAOS-7 model and its updates are available at http://www.spacecenter.dk/files/magnetic-models/CHAOS-7/.

(6) DIFI model is available at https://github.com/CIRES-Geomagnetism/DIFI.

Acknowledgments

This work was supported by the National Natural Science Foundation of China (42250101) and the Macao Foundation. The computation made use of the high-performance computing resources at the center of the MSS data processing and analysis.

References

Backus, G. (1986). Poloidal and toroidal fields in geomagnetic field modeling. *Rev. Geophys.*, *24*(1), 75–109. https://doi.org/10.1029/RG024i001p00075

Carter, J. A., Milan, S. E., Coxon, J. C., Walach, M. T., and Anderson, B. J. (2016). Average field-aligned current configuration parameterized by solar wind conditions. *J. Geophys. Res.: Space Phys.*, *121*(2), 1294–1307. https://doi.org/10.1002/2015JA021567

Chulliat, A., Vigneron, P., and Hulot, G. (2016). First results from the Swarm Dedicated Ionospheric Field Inversion chain. *Earth Planets Space*, *68*(1), 104. https://doi.org/10.1186/s40623-016-0481-6

Edwards, T. R., Weimer, D. R., Olsen, N., Lühr, H., Tobiska, W. K., and Anderson, B.

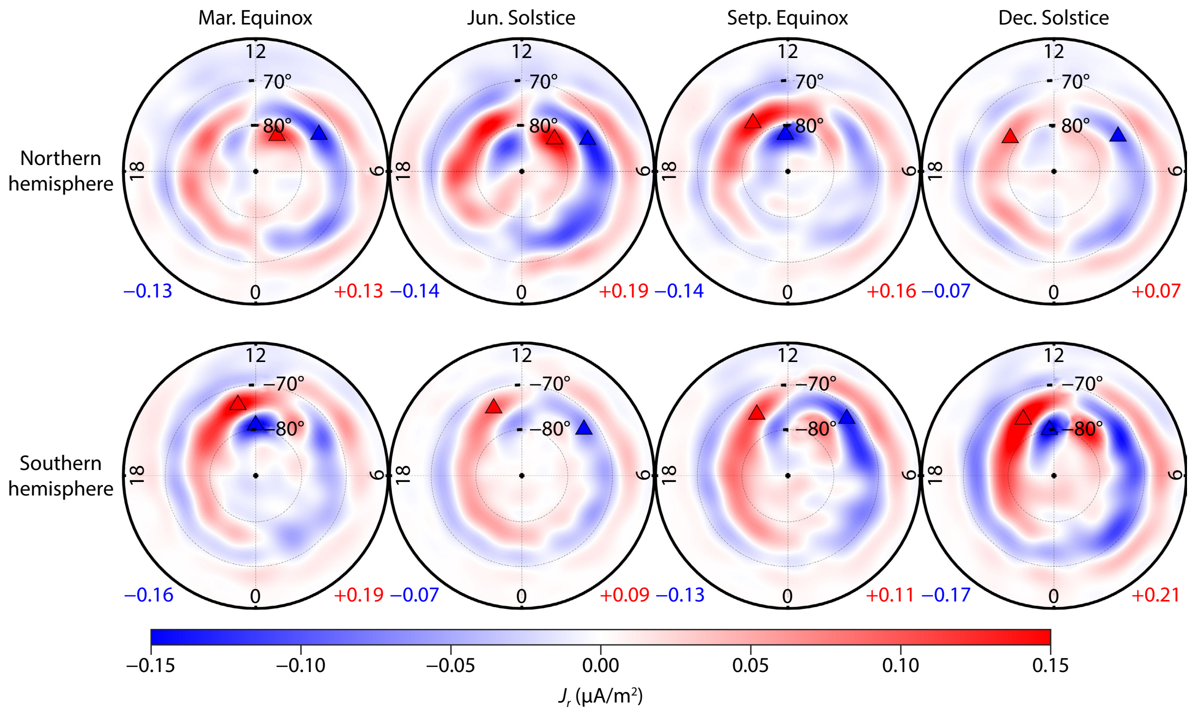

Figure 6. Spatial distribution of field-aligned current densities in the polar regions for the Northern and Southern hemispheres across different seasons, derived from *Model-A*. Each panel presents an orthographic projection of current densities in dipole coordinates poleward of ±60° dipole latitude. Labels on the dashed circle indicate dipole latitudes, while those on the solid circle represent magnetic local times (MLTs: 0, 6, 12, 18). The maximum upward and downward current densities (in μA/m^2) are displayed in the corners, and their locations are marked with colored triangles.

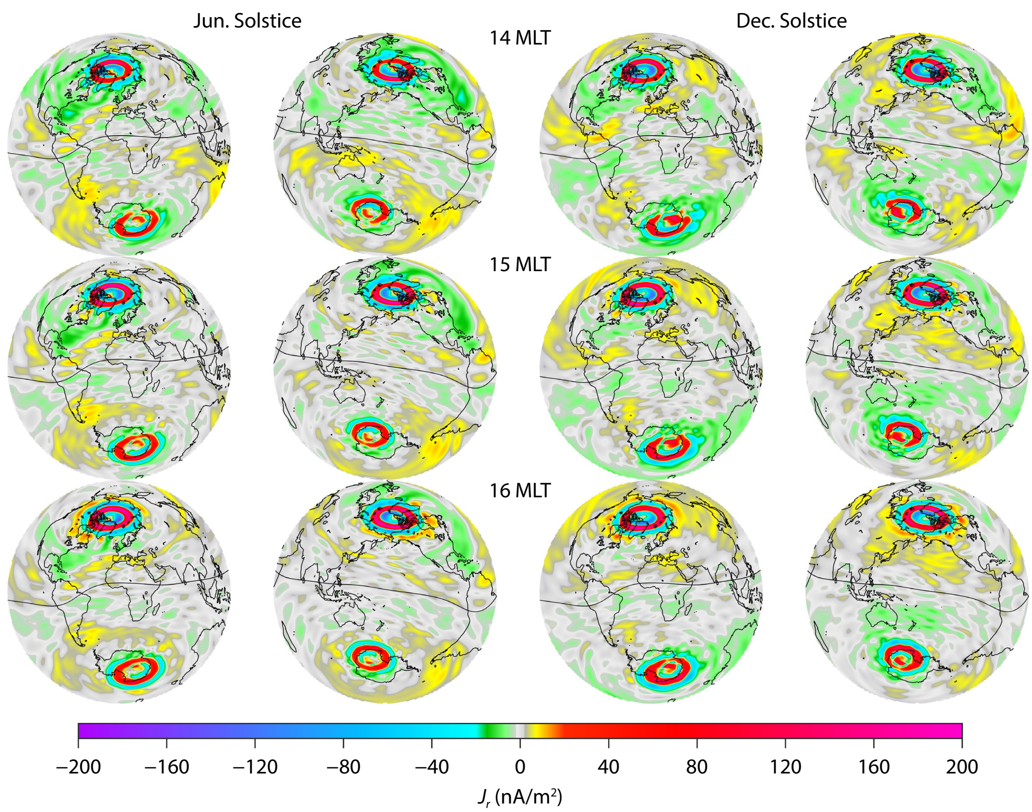

Figure 7. Radial component J_r of the ionospheric F-region currents derived from *Model A* during the June solstice (left pairs) and December solstice (right pairs) for 14:00 MLT to 16:00 MLT. Each pair consists of two azimuthal equidistant projections centred at 0° (left member) and 180° (right member) longitude. Each map represents J_r at a specific MLT across all spatial locations. The magnetic equator is outlined with a black contour.

J. (2020). A third generation field-aligned current model. *J. Geophys. Res.: Space Phys.*, *125*(1), e2019JA027249. https://doi.org/10.1029/2019JA027249
Fillion, M., Hulot, G., Alken, P., and Chulliat, A. (2023). Modeling the climatology of low- and mid-latitude F-region ionospheric currents using the Swarm constellation. *J. Geophys. Res.: Space Phys.*, *128*(5), e2023JA031344. https://doi.org/10.1029/2023JA031344
Finlay, C. C., Lesur, V., Thébault, E., Vervelidou, F., Morschhauser, A., and Shore, R. (2017). Challenges handling magnetospheric and ionospheric signals in internal geomagnetic field modelling. *Space Sci. Rev.*, *206*(1), 157–189. https://doi.org/10.1007/s11214-016-0285-9
Finlay, C. C., Kloss, C., Olsen, N., Hammer, M. D., Tøffner-Clausen, L., Grayver, A., and Kuvshinov, A. (2020). The CHAOS-7 geomagnetic field model and observed changes in the South Atlantic Anomaly. *Earth Planets Space*, *72*(1), 156. https://doi.org/10.1186/S40623-020-01252-9
Fukushima, N. (1994). Some topics and historical episodes in geomagnetism and aeronomy. *J. Geophys. Res.: Space Phys.*, *99*(A10), 19113–19142. https://doi.org/10.1029/94JA00102
Ganushkina, N. Y., Liemohn, M. W., Dubyagin, S., Daglis, I. A., Dandouras, I., De Zeeuw, D. L., Ebihara, Y., Ilie, R., Katus, R., ... Amariutei, O. (2015). Defining and resolving current systems in geospace. *Ann. Geophys.*, *33*(11), 1369–1402. https://doi.org/10.5194/angeo-33-1369-2015
He, M. S., Vogt, J., Lühr, H., Sorbalo, E., Blagau, A., Le, G., and Lu, G. (2012). A high-resolution model of field-aligned currents through empirical orthogonal functions analysis (MFACE). *Geophys. Res. Lett.*, *39*(18), l18105. https://doi.org/10.1029/2012GL053168
Hulot, G., Sabaka, T. J., Olsen, N., and Fournier, A. (2015). The present and future geomagnetic field. In G. Schubert (Ed.), *Treatise on Geophysics* (2nd ed, Vol. 5, pp. 33-78). Oxford: Elsevier. https://doi.org/10.1016/B978-0-444-53802-4.00096-8
Iijima, T., and Potemra, T. A. (1976a). The amplitude distribution of field-aligned currents at northern high latitudes observed by Triad. *J. Geophys. Res.*, *81*(13), 2165–2174. https://doi.org/10.1029/JA081i013p02165
Iijima, T., and Potemra, T. A. (1976b). Field-aligned currents in the dayside cusp observed by Triad. *J. Geophys. Res.*, *81*(34), 5971–5979. https://doi.org/10.1029/JA081i034p05971
Lühr, H., Kervalishvili, G. N., Stolle, C., Rauberg, J., and Michaelis, I. (2019). Average characteristics of low-latitude interhemispheric and F region dynamo currents deduced from the Swarm satellite constellation. *J. Geophys. Res.: Space Phys.*, *124*(12), 10631–10644. https://doi.org/10.1029/2019JA027419
Laundal, K. M., and Richmond, A. D. (2017). Magnetic coordinate systems. *Space Sci. Rev.*, *206*(1), 27–59. https://doi.org/10.1007/s11214-016-0275-y
Laundal, K. M., Finlay, C. C., Olsen, N., and Reistad, J. P. (2018). Solar wind and seasonal influence on ionospheric currents from Swarm and CHAMP measurements. *J. Geophys. Res.: Space Phys.*, *123*(5), 4402–4429. https://doi.org/10.1029/2018JA025387
Matzka, J., Stolle, C., Yamazaki, Y., Bronkalla, O., and Morschhauser, A. (2021). The geomagnetic *Kp* index and derived indices of geomagnetic activity. *Space Wea.*, *19*(5), e2020SW002641. https://doi.org/10.1029/2020SW002641
Newell, P. T., Sotirelis, T., Liou, K., Meng, C. I., and Rich, F. J. (2007). A nearly universal solar wind-magnetosphere coupling function inferred from 10 magnetospheric state variables. *J. Geophys. Res.: Space Phys.*, *112*(A1), A01206. https://doi.org/10.1029/2006JA012015
Ohtani, S., Ueno, G., Higuchi, T., and Kawano, H. (2005). Annual and semiannual variations of the location and intensity of large-scale field-aligned currents. *J. Geophys. Res.: Space Phys.*, *110*(A1), A01216. https://doi.org/10.1029/2004JA010634
Olsen, N. (1997). Ionospheric *F* region currents at middle and low latitudes estimated from Magsat data. *J. Geophys. Res.: Space Phys.*, *102*(A3), 4563–4576. https://doi.org/10.1029/96JA02949
Olsen, N., and Stolle, C. (2012). Satellite geomagnetism. *Annu. Rev. Earth Planet. Sci.*, *40*(1), 441–465. https://doi.org/10.1146/annurev-earth-042711-105540
Olsen, N., Lühr, H., Finlay, C. C., Sabaka, T. J., Michaelis, I., Rauberg, J., and Tøffner-Clausen, L. (2014). The CHAOS-4 geomagnetic field model. *Geophys. J. Int.*, *197*(2), 815–827. https://doi.org/10.1093/gji/ggu033
Park, J., Yamazaki, Y., and Lühr, H. (2020). Latitude dependence of interhemispheric field-aligned currents (IHFACs) as observed by the Swarm constellation. *J. Geophys. Res.: Space Phys.*, *125*(2), e2019JA027694. https://doi.org/10.1029/2019JA027694
Richmond, A. D. (1995). Ionospheric electrodynamics using Magnetic Apex Coordinates. *J. Geomagn. Geoelectr.*, *47*(2), 191–212. https://doi.org/10.5636/jgg.47.191
Sabaka, T. J., Olsen, N., and Langel, R. A. (2000). A comprehensive model of the near-earth magnetic field. National Aeronautics and Space Administration, Goddard Space Flight Center.
Sabaka, T. J., Olsen, N., and Langel, R. A. (2002). A comprehensive model of the quiet-time, near-Earth magnetic field: Phase 3. *Geophys. J. Int.*, *151*(1), 32–68. https://doi.org/10.1046/j.1365-246X.2002.01774.x
Sabaka, T. J., Olsen, N., Tyler, R. H., and Kuvshinov, A. (2015). CM5, a pre-Swarm comprehensive geomagnetic field model derived from over 12 yr of CHAMP, Ørsted, SAC-C and observatory data. *Geophys. J. Int.*, *200*(3), 1596–1626. https://doi.org/10.1093/gji/ggu493
Sabaka, T. J., Tøffner-Clausen, L., Olsen, N., and Finlay, C. C. (2020). CM6: A comprehensive geomagnetic field model derived from both CHAMP and Swarm satellite observations. *Earth Planets Space*, *72*(1), 80. https://doi.org/10.1186/s40623-020-01210-5
Stauning, P. (2002). Field-aligned ionospheric current systems observed from Magsat and Oersted satellites during northward IMF. *Geophys. Res. Lett.*, *29*(15), ORS 6-1–ORS 6-4. https://doi.org/10.1029/2001GL013961
Thébault, E., Finlay, C. C., Beggan, C. D., Alken, P., Aubert, J., Barrois, O., Bertrand, F., Bondar, T., Boness, A., ... Zvereva, T. (2015). International geomagnetic reference field: The 12th generation. *Earth Planets Space*, *67*(1), 79. https://doi.org/10.1186/s40623-015-0228-9
van Sabben, D. (1966). Magnetospheric currents, associated with the N-S asymmetry of S_q. *J. Atmos. Terr. Phys.*, *28*(10), 965–982. https://doi.org/10.1016/S0021-9169(17)30026-0
van Sabben, D. (1970). Solstitial S_q-currents through the magnetosphere. *J. Atmos. Terr. Phys.*, *32*(7), 1331–1336. https://doi.org/10.1016/0021-9169(70)90064-4
Wang, F. J., Lühr, H., Xiong, C., and Zhou, Y. L. (2022). Improved field-aligned current and radial current estimates at low and middle latitudes deduced by the Swarm dual-spacecraft. *J. Geophys. Res.: Space Phys.*, *127*(6), e2022JA030396. https://doi.org/10.1029/2022JA030396
Winch, D. E., Ivers, D. J., Turner, J. P. R., and Stening, R. J. (2005). Geomagnetism and Schmidt quasi-normalization. *Geophys. J. Int.*, *160*(2), 487–504. https://doi.org/10.1111/j.1365-246X.2004.02472.x
Xiong, C., Wang, S. M., Lühr, H., Wang, F. J., and Zhou, Y. L. (2023). Influence of the polar electrojet on field-aligned current estimates from single satellite magnetic field measurements. *J. Geophys. Res.: Space Phys.*, *128*(7), e2023JA031472. https://doi.org/10.1029/2023JA031472
Zhang, K. (2023). A novel geomagnetic satellite constellation: Science and applications. *Earth Planet. Phys.*, *7*(1), 4–21. https://doi.org/10.26464/epp2023019